*Journal of Applied Fluid Mechanics*, Vol. 18, No. 11, pp. 2874-2892, 2025.
Available online at www.jafmonline.net, ISSN 1735-3572, EISSN 1735-3645.
https://doi.org/10.47176/jafm.18.11.3433

# Improving Flow Stability of a Centrifugal Compressor by Regulating Energy Transfer Among Dynamic Modes

X. A. Xie[1], Z. X. Liu[1,2], X. J. Li[1,2†], M. Zhao[1,2] and Y. J. Zhao[3]

[1] *School of Mechanical Engineering, Tianjin University, 300350 Tianjin, China*
[2] *National Key Laboratory of Vehicle Power System, Tianjin University, 300350 Tianjin, China*
[3] *School of Mechanical Engineering, Tianjin University of Commerce, 300134 Tianjin, China*

†*Corresponding Author Email: lixiaojian@tju.edu.cn*

## ABSTRACT

Compressor flow instability significantly constrains the development of aviation power systems. Improving flow stability of compressor is usually challenging without deteriorating aerodynamic performances. In this study, a new method for improving compressor flow stability is proposed based on regulating energy transfer among flow field dynamic modes. Firstly, dynamic mode decomposition (DMD) is conducted on the compressor flow field to identify the dominant dynamic modes and the corresponding evolution characteristics. It is found that the BPF (Blade-Passing-Frequency) mode and its harmonics represent the rotor-stator interactions of the flow field, and they are named as inherent mode. The 0.11RF (Rotor Frequency) mode, which is caused by large-scale low-frequency disturbances downstream of the rotor, characterizes periodic fluctuations of the compressor flow field, and it is recognized as characteristic mode. DMD analyses on the compressor throttling process reveals that the essential feature of compressor flow instability is the energy transfer from the inherent mode to the characteristic mode. Then, an optimization method is proposed for improving flow stability by maximizing inherent mode energy and minimizing characteristic mode energy. Optimization based on this approach has resulted in a 25.4% increase in the energy-ratio of the inherent mode at the compressor near-stall condition, alongside a 51.84% reduction in the energy-ratio of the characteristic mode. The compressor stall flow rate is decreased by 8.45% and the choke flow rate is increased by 5.11%, and the overall aerodynamic performances are maintained.

***Article History***

*Received February 10, 2025*
*Revised April 26, 2025*
*Accepted June 8, 2025*
*Available online September 3, 2025*

***Keywords:***

*Compressor*
*Flow stability improvement*
*Dynamic mode decomposition*
*Inherent and characteristic modes*
*Mode energy transfer regulation*

## 1. INTRODUCTION

As a critical boosting component in turboprop engines, turbojet engines, and gas turbines, compressor plays a key role in the overall performance and reliability of the engine (Li et al., 2021; Hosseinimaab & Tousi, 2022). Over the past several decades, the pursuit of high-performance engines has driven compressors towards high rotating speed, high pressure ratio, and small size, resulting in more complex internal flow phenomena that deteriorate the flow stability (Li et al., 2022; Yang et al., 2022). This challenge has become a major bottleneck in the development of aircraft engines, making the study of compressor flow stability more and more crucial. In compressor flow stability investigations, the core issues primarily focus on two key aspects. The first one is understanding the fundamental mechanisms of compressor flow instability. And the second is developing stability-enhancement methods based on the gained mechanism insights.

In terms of understanding flow mechanisms, researchers have developed different analysis approaches: steady-state analysis method, local flow analysis method, global stability modeling method, and global data-driven analysis method. The steady-state analysis method is usually used for preliminary or fast analysis of compressor flow stability. For example, D-factor is a critical parameter associated with flow stability in compressor design (Huang et al., 2020). It reflects the adverse pressure gradient on the suction side of the blades during the deceleration in the diffusion section (Xu et al., 2022). The stability parameter (*SP*) is defined as the derivative of the static pressure ratio concerning mass flow rate for compressor (Shu et al., 2018). The positive and negative of *SP* can be used to judge the stability of various

**NOMENCLATURE**

| | | | |
|---|---|---|---|
| $\eta$ | efficiency | FFT | Fast Fourier transform |
| $\varepsilon$ | pressure ratio | PS | Pressure Surface |
| $E_C$ | characteristic mode energy-ratio | PV | Passage Vortex |
| $E_I$ | inherent mode energy-ratio | RANS | Reynolds-Averaged Navier-Stokes |
| *SP* | Stability Parameter | RF | Rotor Frequency |
| BPF | Blade Passing Frequency | SST | Shear Stress Transport |
| BTLF | Blade Tip Leakage Flow | SVD | Singular Value Decomposition |
| BTLV | Blade Tip Leakage Vortex | URANS | Unsteady Reynolds-Averaged Navier-Stokes |
| DMD | Dynamic-Mode-Decomposition | | |

components of compressor (Xu et al., 2023). However, these methods typically assess compressor stability from a steady-state perspective. In the near-stall condition of high-speed compressors, strong three-dimensional unsteady characteristics arise within the flow passage. Therefore, analyzing compressor flow stability solely from a steady-state viewpoint will introduce significant uncertainty.

In order to gain a deeper understanding of compressor flow stability mechanisms, many studies have shifted their focuses to the unsteady evolution of local flow structures. For instance, a classic criterion for compressor instability is leading-edge spillage or trailing-edge backflow (Stein et al., 2025). Specifically, the blade tip leakage flow (BTLF) reaching the leading edge of adjacent main blades, or the outlet fluid flowing back to the trailing edge of adjacent blades suggests the inception of compressor instability. Cameron et al. Cameron et al. (2013) studied BTLF and confirmed that leading-edge spillage can lead to compressor instability by breaking the balance of the axial momentum flux of the blade tip leakage reverse flow and the main flow. Grondin et al. (2018) observed that a vortex resembling a tornado generates as a result of the flow separation at the leading edge of the impeller, and propagates around the circumference. This indicates that the cause of compressor instability is flow separation rather than tip leakage vortex spillage. It is clear that the above studies focus solely on local unsteady flow structures, resulting in varying understandings of instability mechanisms across different compressors (Fujisawa et al., 2019; Zhang et al., 2022), and the essence of flow instability cannot be obtained from a global perspective.

Additionally, some researchers have elucidated the instability mechanisms of compressors by analyzing the evolution of flow disturbances based on global stability modeling methods. For example, the Moore-Greitzer model (Bitikofer et al., 2017; Wilson, 2024) has theoretically predicted the existence of large-scale circumferential rotating disturbance waves in compressor cascade. Cheng et al. (2017) and Dong et al. (2018) considered the three-dimensional characteristics of compressor instability and developed a compressible linear stability model based on the Euler equations and eigenvalue theory. Sun et al. (2013) and Liu et al. (2014, 2015) developed various body-force models, and predicted the onset of flow instability in axial and centrifugal compressors. However, due to the complexity of the equations to be solved, these studies generally make assumptions of inviscid flow and linearization. This inevitably reduces the accuracy of the models when describing the development of compressor instability.

In recent years, global data-driven analysis methods have been progressively developed and applied to investigate compressor instability mechanisms. Thid kind of methods implement the analysis of flow instability mechanisms from a global perspective, and the typical representative is the dynamic mode decomposition (DMD) method (Schmid, 2010). So far, researchers have employed the DMD method to investigate the unsteady characteristics of compressors, and have identified the flow structures associated with compressor instability (Xue & Tong, 2019; Zhu et al., 2019; Hu et al., 2020a). Due to the spatial uncertainty of instability in compressors, instability modes extracted from different compressors are distributed across various components, such as impeller (Xue et al., 2019), volute (Fu et al., 2020), and diffuser (Hu et al., 2020b). These studies demonstrate that the DMD method is highly effective in capturing the global unsteady flow characteristics of compressors (Broatch et al., 2019), and can help to gain a more comprehensive understanding of instability mechanisms.

The second aspect regarding compressor instability study concentrates on stability enhancement methods. Zhao et al. (2023) conducted a stability-enhancement optimization for the compressor based on steady-state numerical simulations. It is found that the stable flow range is expanded by 2.7 percentage points. Hong et al. (2018) found that the large-scale leakage vortex has a great influence on compressor instability. By implementing unsteady jet control technology at the blade tip region, the compressor flow stability has been enhanced. Xu et al. (2019) proposed a stall warning approach based on aero-acoustic theory and developed the stall precursor-suppressed casing treatment, which has successfully enhanced the compressor flow stability. Recent studies have begun to investigate the correlation between global dynamic modes and geometric parameters of compressors based on DMD analysis on three-dimensional unsteady flow fields (Zhou et al., 2025). However, no attempts have been made to achieve stability enhancement of compressor through dynamic modes regulations.

In summary, previous studies usually analyze the compressor instability mechanisms from the steady or local perspective, or based on simplified theoretical models. According to the gained mechanisms, different

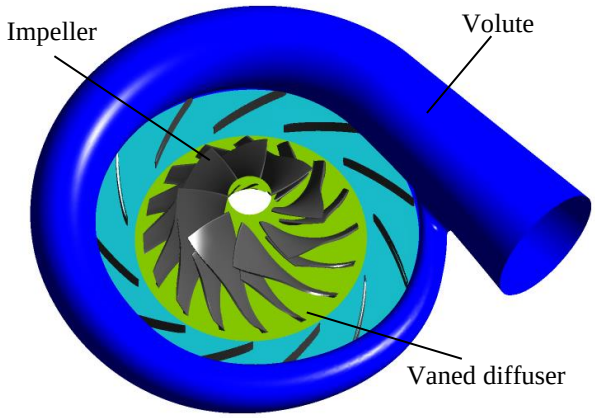


**Fig. 1 Three-dimensional geometry model**

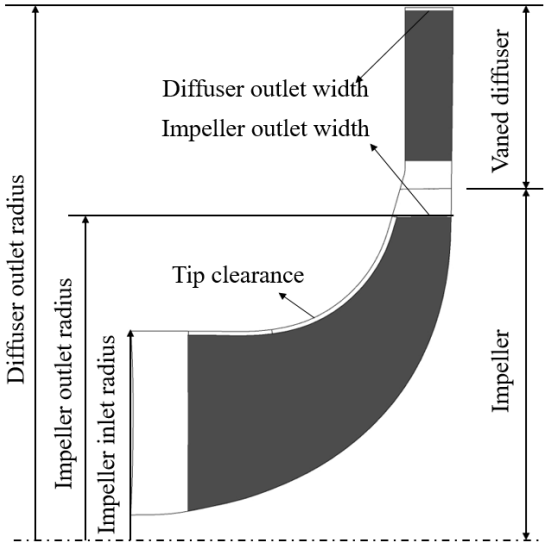


**Fig. 2 Meridional section of the impeller and diffuser**

flow stability enhancement methods have been developed. However, due to inherent limitations in the mechanisms understanding, these methods are usually not so efficient and robust. This might be the main reason for the fact that flow stability and aerodynamic performances of compressors cannot be improved simultaneously. DMD method has provided an efficient way to comprehensively understand the global unsteady mechanisms of compressor instability, based on the mechanisms, it is possible to develop a better stability enhancement method for compressors.

In this study, the DMD method is introduced to analyze the global and unsteady mechanisms of compressor flow instability. Then a novel method is proposed to enhance compressor flow stability by regulating the energy transfer between dominant dynamic modes. This method is expected to significantly improve the compressor stall margin while maintaining its aerodynamic performances.

**Table 1 Specifications of the compressor**

| Parameters | Values |
|---|---|
| Design rotating speed | 50000 rpm |
| Tip clearance | 0.85 mm |
| Full/splitter blades number | 8/8 |
| Impeller inlet radius | 50mm |
| Impeller outlet radius | 72.5 mm |
| Impeller outlet width | 11.8 mm |
| Diffuser vanes number | 11 |
| Diffuser outlet radius | 113 mm |
| Diffuser outlet width | 9.2 mm |

## 2. COMPRESSOR AND NUMERICAL METHOD

The model to be studied is a centrifugal compressor. The three-dimensional geometry model is illustrated in Fig. 1, the meridional section of the impeller and diffuser is shown in Fig.2, and the main design parameters are listed in Table 1.

A single-passage numerical simulation is performed on the compressor, the computational domain includes the impeller, diffuser, and volute. The governing equations are the Reynolds-Averaged Navier-Stokes (RANS) equations. The *k-ω* SST (Shear Stress Transport) model is used for turbulence modeling. This turbulence model demonstrates excellent capabilities for near-wall treatment and separation prediction, hence, it is extensively used in numerical simulations of centrifugal compressors (Zhang et al., 2023). The impeller and diffuser are discretized with structured grids, using O-shaped grids around the blades and H-shaped grids in other regions. The volute adopts an unstructured mesh. The first layer of the grid near solid walls satisfies $y+\leq 3$, meeting the computational requirements of the *k-ω* SST model. The inlet boundary conditions employ total temperature and total pressure, while the outlet boundary condition is defined by mass flow rate. Periodic boundary conditions are used in the circumferential direction of the single-passage domain. The frozen rotor method is applied at the interface between the stator and rotor, and adiabatic no-slip boundary conditions are used for solid walls. The governing equations and turbulence model are discretized based on the finite volume method. The High-Resolution scheme (Ansys, 2011) is employed for spatial discretization, and the implicit second-order backward Euler scheme is employed for temporal discretization.

A study on grid independence is performed. Three grids with coarse, medium, and fine densities are generated. The grid density for the impeller and diffuser is modified by altering the grid nodes in both the spanwise and streamwise directions. For volute mesh, adjustments are made to the maximum grid size and the growth rate of the grid near the wall. Comprehensive details regarding these grids can be found in Table 2. Figure 3 presents the characteristic curves for the simulations with different grids. It shows that the medium grid satisfies the requirements of grid independence. Consequently, the subsequent numerical simulations are all based on this

**Table 2 Elements numbers of the three meshes**

| | Impeller | Diffuser | Volute | Compressor |
|---|---|---|---|---|
| Coarse | $56\times10^4$ | $18\times10^4$ | $157\times10^4$ | $231\times10^4$ |
| Medium | $81\times10^4$ | $30\times10^4$ | $211\times10^4$ | $322\times10^4$ |
| Fine | $162\times10^4$ | $45\times10^4$ | $308\times10^4$ | $515\times10^4$ |

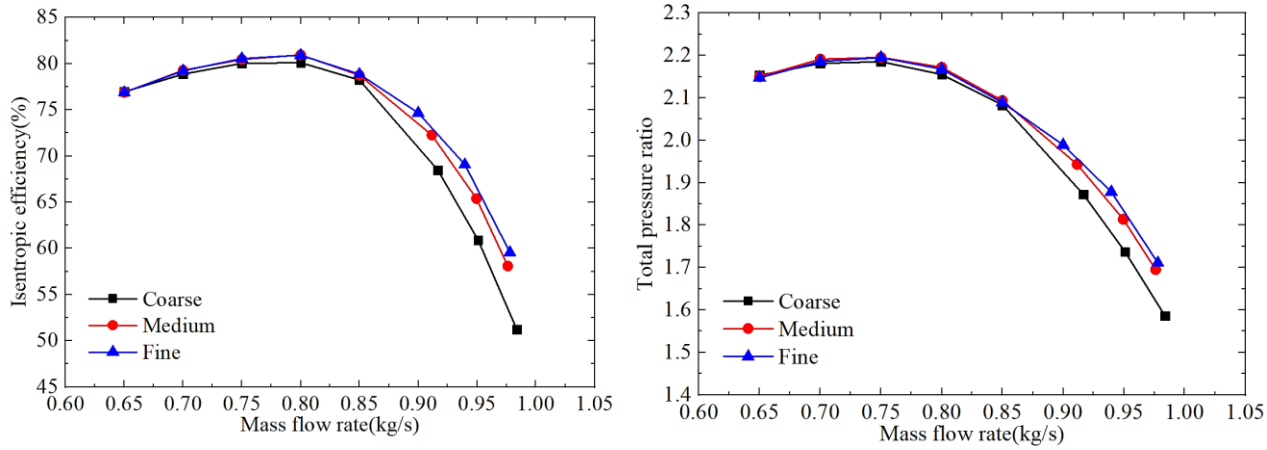


(a) isentropic efficiency (b) total pressure ratio

**Fig. 3 Characteristics of the compressor with different grids**

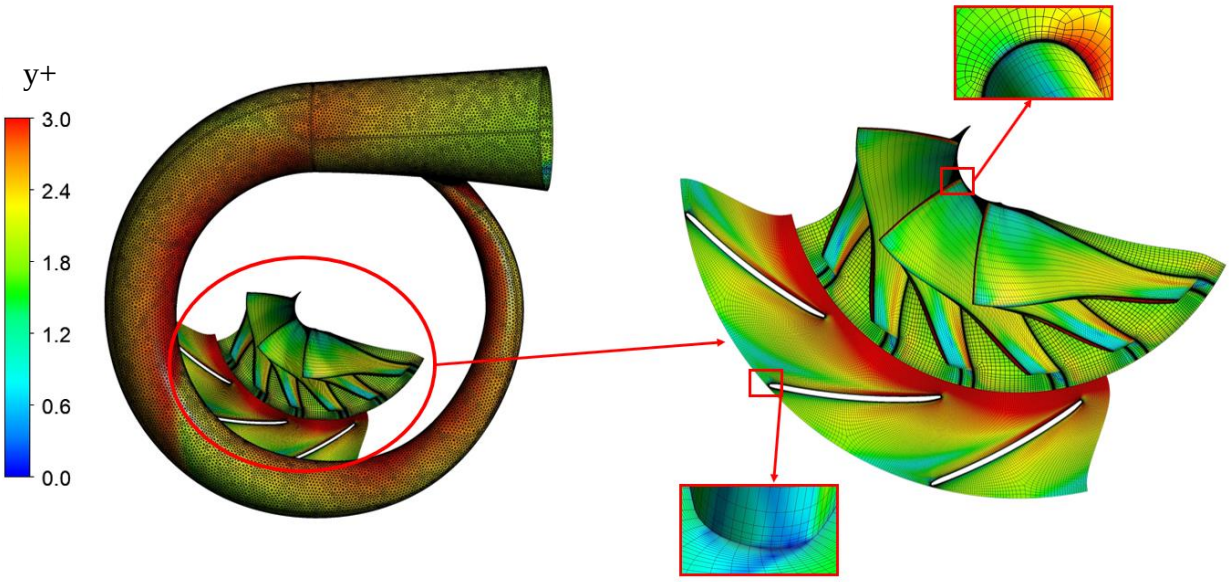


**Fig. 4 Medium grid of the compressor**

grid. Figure 4 displays the overall view and the partial enlargements of the medium grid, where the y+ distribution is also illustrated, which conforms the rationality of the grid structure

Based on the medium grid, unsteady numerical simulation is conducted for the compressor. For the unsteady calculation, the governing equations are the URANS (Unsteady Reynolds-Averaged Navier-Stokes) equations. The interface between the stator and rotor employs the Transient Rotor Stator method. The blade passing through a single-passage comprises 20 timesteps, each timestep is 1/160$T$, where $T$ is the rotor rotational period.

The unsteady simulation results of the compressor are compared to the experimental data. The original compressor is supplied by Dalian Maritime University, and its aerodynamic performances are evaluated using an in-house turbocharger testing facility. Pressure sensors and thermocouples are positioned at the impeller inlet and volute outlet. Measurements of total pressure and total temperature at these locations are taken to calculate the total pressure ratio and isentropic efficiency of the compressor. During the experiment, the compressor mass

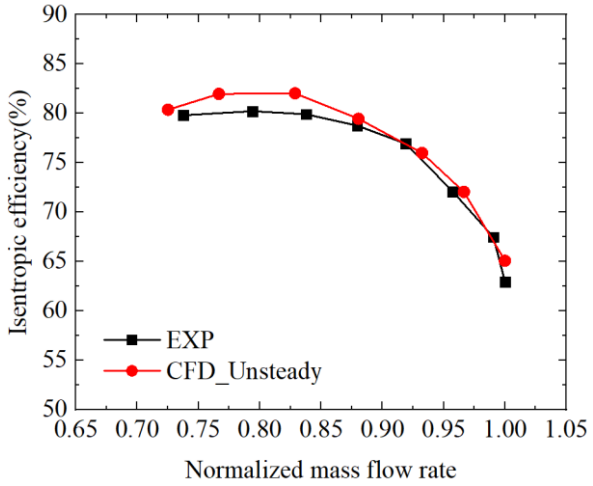


(a) isentropic efficiency

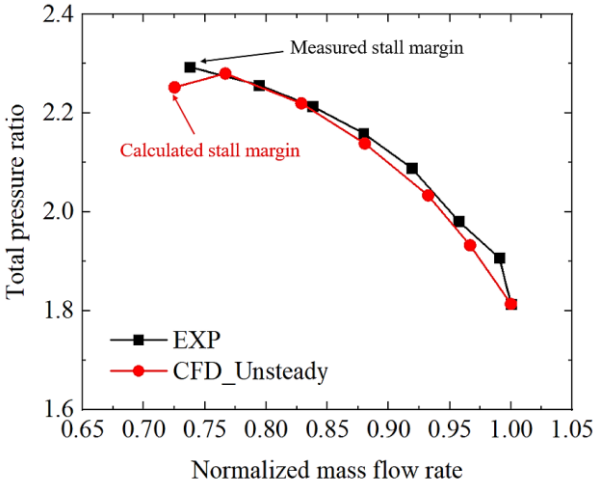


(b) total pressure ratio

**Fig. 5 Calculated and measured characteristics of the compressor**

flow rate is gradually reduced by an outlet throttle valve, the measurement is stopped when the stall occurs (it is usually accompanied by the significant vibration of the test bench and the appearance of cacophony from the compressor) (Day, 2016).

Figure 5 presents a comparison of the characteristic curves of the compressor between measurement and calculation. The efficiency and pressure ratio are time-averaged results of the unsteady simulation results. As illustrated in Fig. 5, the leftmost point on the experimental characteristic curve represents the measured stall margin, since the stall state is very unstable, the smaller flow rate of the compressor is not measured. The leftmost point on the simulated characteristic curve denotes the calculated stall margin. Figure 6 shows the streamline of the tip leakage flow under the calculated stall margin point. As shown in the figure, the tip leakage flow is nearly parallel to the impeller inlet, and leading-edge spillage is about to occur (Vo et al., 2005), but it is still stable. Therefore, this condition is regarded as the calculated stall boundary. The relative error of the measured stall margin and the

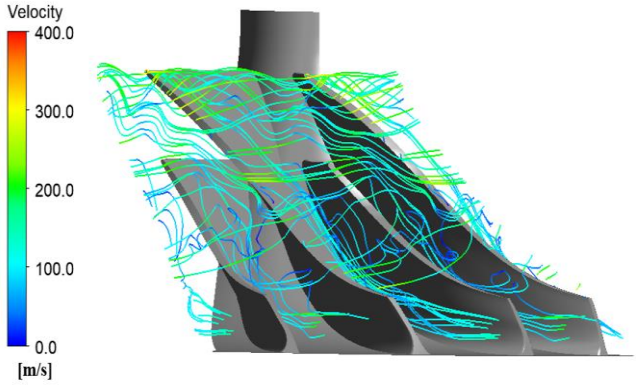


**Fig. 6 Streamline of the tip leakage flow under the calculated stall margin point**

calculated stall margin is 2.94%, the relative errors of efficiency and pressure ratio at the stall margin condition are 0.7% and 1.78% respectively. In addition to the near-stall condition, the performance curves show consistent trends between experiment and calculation, the maximum relative errors of the efficiency and pressure ratio are 2.19% and 1.78%. This indicates that the numerical method is reliable and can obtain relatively accurate unsteady flow fields of the compressor for further DMD analyses.

## 3. DYNAMIC MODE DECOMPOSITION METHOD

The theoretical framework of the dynamic mode decomposition (DMD) method employed in this study is introduced. DMD is an emerging data-driven approach that can capture the global dynamic characteristics of unsteady flow fields. In recent years, it has been gradually incorporated into the analysis of compressor flow mechanisms and has been proven to be a superior method for analyzing unstable flows. The DMD method has evolved from the overall stability analysis of the Koopman operator (Kou & Zhang, 2017; Li et al., 2023), serving as a powerful tool that uses linear techniques to analyze the nonlinear dynamic characteristics of flow fields. It can rapidly extract dynamic information from large datasets, making it highly effective for complex flow analysis (Bagheri, 2013; Taira et al., 2017). The theoretical derivation of the DMD method is presented below.

The snapshots of the unsteady flow field obtained from numerical simulations can be expressed as $\{x_1, x_2, x_3 \cdots, x_n\}$, where $x_i \in \mathbb{C}^m$ represents the spatial field data at the $i^{\text{th}}$ time instant, which contains $m$ spatial points, and $n$ is the number of snapshots, with each snapshot taken at a time interval of $\Delta t$. Assuming there exists a linear operator $\boldsymbol{A}$ that connects the flow fields at two adjacent time instances:

$$x_{i+1} = \boldsymbol{A} x_i \tag{1}$$

The data sequence among $n$ time instants can be divided into two matrices, $\boldsymbol{X}$ and $\boldsymbol{Y}$:

$$\begin{aligned} X &= [x_1\ x_2\ x_3\ \cdots\ x_{n-1}] \\ Y &= [x_2\ x_3\ x_4\ \cdots\ x_n] \in \mathbb{C}^{m\times(n-1)} \end{aligned} \tag{2}$$

According to the linear assumption in Eq. (1), the relationship between the matrices $\boldsymbol{X}$ and $\boldsymbol{Y}$ satisfies the following equation:

$$\boldsymbol{Y} = \boldsymbol{AX} \tag{3}$$

According to Eq. (3), the system matrix $\boldsymbol{A}$ can be expressed as:

$$\boldsymbol{A} = \boldsymbol{YX}^{\dagger} \tag{4}$$

where $\boldsymbol{X}^{\dagger}$ represents the Moore-Penrose pseudoinverse of matrix $\boldsymbol{X}$ (Tu et al., 2014).

Performing the singular value decomposition (SVD) (Schmid, 2010) of matrix $\boldsymbol{X}$, it yields:

$$\boldsymbol{X} = \boldsymbol{U\Sigma V}^{\mathrm{H}} \tag{5}$$

where $\boldsymbol{U} \in \mathbb{C}^{m\times r}$ is a unitary matrix containing the left singular vectors of $\boldsymbol{X}$, $\boldsymbol{\Sigma} \in \mathbb{C}^{r\times r}$ is a diagonal matrix with the singular values of $\boldsymbol{X}$, $\boldsymbol{V} \in \mathbb{C}^{r\times n}$ is the unitary matrix which contains the right singular vectors of $\boldsymbol{X}$. Thus, $\boldsymbol{X}^{\dagger}$ can be expressed as:

$$\boldsymbol{X}^{\dagger} = \boldsymbol{V\Sigma}^{-1}\boldsymbol{U}^{\mathrm{H}} \tag{6}$$

Substituting Eq. (6) into Eq. (4) yields:

$$\boldsymbol{A} = \boldsymbol{YV\Sigma}^{-1}\boldsymbol{U}^{\mathrm{H}} \tag{7}$$

By applying a similarity transformation to matrix $\boldsymbol{A}$ using matrix $\boldsymbol{U}$, the reduced-order matrix $\tilde{\boldsymbol{A}}$ can be obtained as follows:

$$\tilde{\boldsymbol{A}} = \boldsymbol{U}^{H}\boldsymbol{AU} = \boldsymbol{U}^{H}\boldsymbol{YV}\Sigma^{-1} \tag{8}$$

Performing the eigen decomposition of the reduced-order matrix $\tilde{\boldsymbol{A}}$ yields:

$$\tilde{\boldsymbol{A}}W = \boldsymbol{W\Lambda}, \quad \boldsymbol{\Lambda} = \mathrm{diag}(\lambda_1, \lambda_2, \cdots, \lambda_r) \tag{9}$$

where $\boldsymbol{\Lambda}$ is the diagonal matrix formed by the eigenvalues of $\tilde{\boldsymbol{A}}$, with its corresponding eigenvectors constituting the columns of matrix $\boldsymbol{W}$. Combining Eq. (7) and Eq. (8), Eq. (9) can be rewritten as:

$$\boldsymbol{AYV\Sigma^{-1}W} = \boldsymbol{YV\Sigma^{-1}W\Lambda} \tag{10}$$

The modes $\boldsymbol{\Phi} = [\boldsymbol{\Phi}_1, \boldsymbol{\Phi}_2, \cdots, \boldsymbol{\Phi}_r]$ can be defined as follows:

$$\boldsymbol{\Phi} = \boldsymbol{YV\Sigma^{-1}W} \tag{11}$$

Then Eq. (10) can be written as:

$$\boldsymbol{A\Phi} = \boldsymbol{\Phi\Lambda} \tag{12}$$

The vector $\boldsymbol{\Phi}$ is the eigenvector of matrix $\boldsymbol{A}$ (DMD mode). The growth rate and physical frequency of the $i^{\mathrm{th}}$ order mode are defined as follows:

$$\begin{aligned} \sigma_i &= \frac{\ln\left(|\lambda_i|\right)}{\Delta t} \\ \omega_i &= \frac{\arg\left(\lambda_i\right)}{\Delta t} \end{aligned} \tag{13}$$

The amplitude vector $\boldsymbol{\alpha}$ of the modes is defined as:

$$\boldsymbol{\Phi\alpha} = x_1 \tag{14}$$

It can be calculated by the least-squares method (Wu *et al.* 2021) as follows:

$$\boldsymbol{\alpha} = \boldsymbol{\Phi}^{-1}x_1 \tag{15}$$

And the modulus of the vector represents the energy of the corresponding DMD mode is:

$$E_i = |\alpha_i|^2 \tag{16}$$

where $E_i$ is the energy of the $i^{\mathrm{th}}$ mode. The energy-ratio of mode can be defined as follows:

$$ER_i = \frac{E_i}{\sum_{i=1}^{r} E_i} \tag{17}$$

where $ER_i$ is the energy-ratio of the $i^{\mathrm{th}}$ mode. For convenience, $ER$ is usually normalized to be 0~1.

## 4. DYNAMIC CHARACTERISTICS OF FLOW INSTABILITIES

Dynamic mode analyses are carried out for the unsteady flow fields of the compressor. The physical explanations of single-frequency modes are clarified through the coupling analyses of unsteady flow structures. Then the correlations between flow instability and energy transfers among dynamic modes are explored.

### 4.1 Overall Characteristics of Mode Patterns

To determine which component of the centrifugal compressor becomes unstable first during throttling process, the stability of each component is analyzed using the *SP* criterion (Shu et al., 2018). The *SP* is defined as the gradient of the pressure ratio versus mass flow rate for each component. The equation is as follows:

$$SP_i = \frac{\partial \pi_i}{\partial m} \approx \frac{\pi_{i,2} - \pi_{i,1}}{m_2 - m_1} \tag{18}$$

where $m$ and $\pi$ represent the mass flow rate and total-to-static pressure ratio respectively, subscript $i$ denotes the index of the components within the compressor, subscripts 1 and 2 are two neighboring operating conditions on the characteristic curves. A negative *SP* suggests that the flow field within the component is stable; conversely, a positive *SP* suggests that it has already become unstable. The *SP* essentially reflects the negative slope of the total-to-static pressure ratio

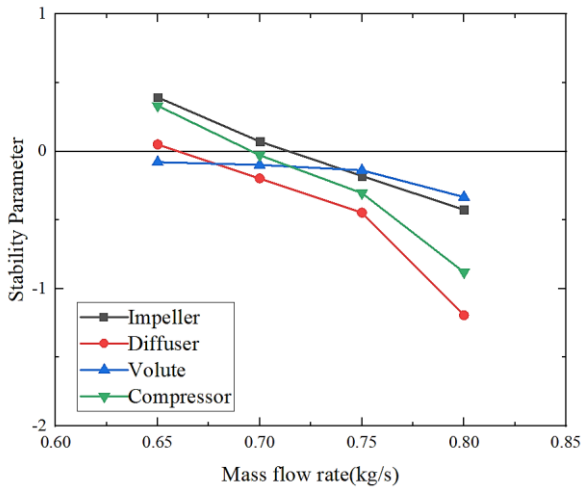


**Fig. 7 Stability parameters of the compressor and its components in small flow rate region**

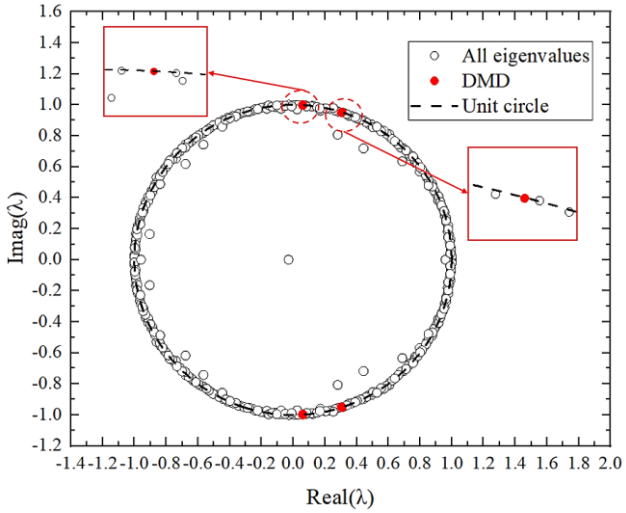


**Fig. 8 Eigenvalues of dominant DMD modes under the 0.74kg/s operating condition**

characteristic curve of compressors, it is usually used in small flow rate region, where the flow instability is likely to occur. And it normally makes no sense when applied to the large flow rate region (near choke), as there are no flow instability problems in compressors (Cumpsty, 2004).

Figure 7 shows the stability parameters of the compressor and its components in small flow rate region (smaller than the design mass flow rate). It can be observed from the figure that when the mass flow rate of the compressor drops below 0.7kg/s, the instability firstly occurs in the impeller, and then the instability appears in the compressor. However, instability in the diffuser flow field does not occur until the mass flow rate decreases to 0.65kg/s, at which point the instability of the impeller and the entire compressor worsens. The volute, on the other hand, remains stable throughout the entire operating range. This indicates that the instability of the centrifugal compressor is mainly attributed to the impeller instability. Therefore, the following analyses will focus on the flow field within the impeller.

DMD analyses are performed for the static pressure field at the 95% span of the impeller. This cross-section contains 16,832 grid points (the spatial dimension of DMD system matrix $\boldsymbol{A}$). The sampling period covers 9 rotor rotations and a total of 360 flow field snapshots (the temporal dimension of DMD system matrix $\boldsymbol{A}$). The time interval between the flow field snapshots is $1/40T$ ($T$ is the rotor rotation period). The mode frequencies are calculated by Eq. (13), with frequencies normalized by rotor frequency (RF), and the energy-ratios are calculated by Eq. (17).

DMD analyses are carried out under different operating conditions (0.74kg/s, 0.7kg/s and 0.65kg/s). Figures 8, 9, 10 show the eigenvalues distributions of DMD modes under the 0.74kg/s, 0.7kg/s and 0.65kg/s operating conditions, respectively. The eigenvalues of the dominant modes are highlighted in red. As can be seen in the figure, all the chosen modes are close to the unit circle, confirming that they are stable. The growth rates of these modes are almost equal to zero, and their temporal

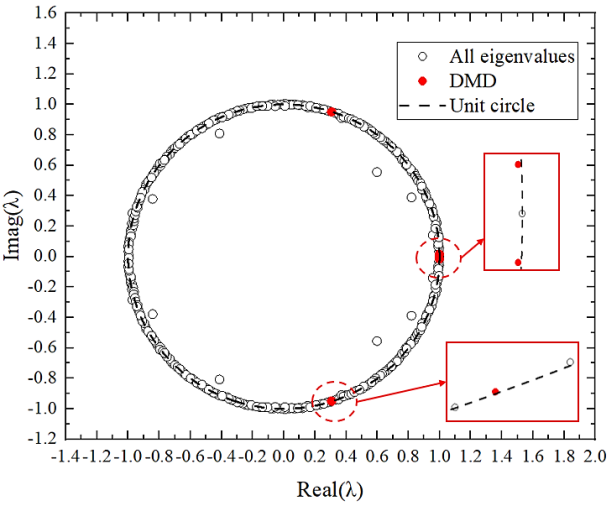


**Fig. 9 Eigenvalues of dominant DMD modes under the 0.7kg/s operating condition**

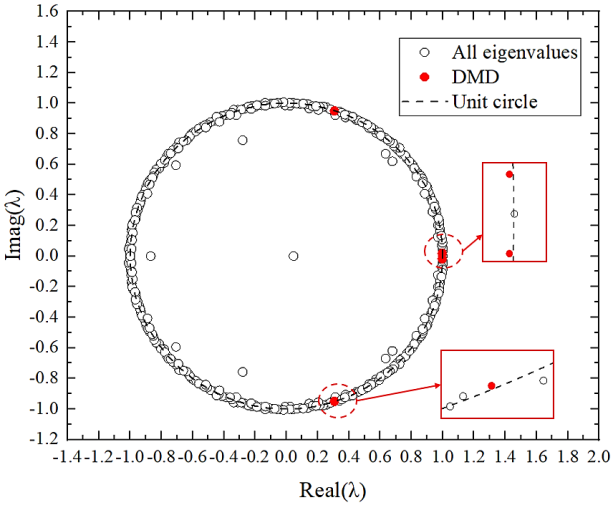


**Fig. 10 Eigenvalues of dominant DMD modes under the 0.65kg/s operating condition**

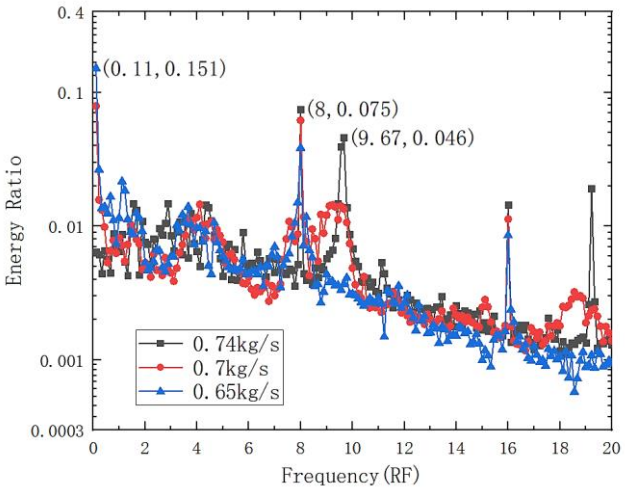


**Fig. 11 Comparison of mode frequency spectrums of the compressor impeller at 95% span under different operating conditions**

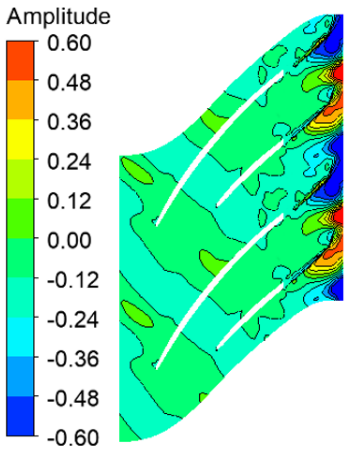


**Fig. 12 BPF mode of the compressor impeller at 95% span under the 0.74kg/s operating condition**

evolutions nearly present periodic fluctuations. This is explainable. The unsteady flow fields of the compressor used for DMD analyses are obtained by specifying fixed outlet boundary conditions (i.e., 0.74kg/s, 0.7kg/s and 0.65kg/s), hence, after the simulations are converged, the flow fields tend to fluctuate periodically. It also confirms that the DMD results are reliable. Note that the DMD modes and the corresponding amplitudes under different operating conditions are different, therefore, the modes energy transfer between them under various operating conditions can be discussed.

Figure 11 compares the mode frequency spectrums of the compressor impeller at 95% span under different operating conditions. It shows that three mode frequencies stand out with significantly higher energy-ratios than the others under different operating conditions. These frequencies are 0.11RF, BPF (blade passing frequency), and 9.67RF. As the compressor flow rate decreases, the mode energy-ratio of the BPF (=8RF) decreases slightly, and the energy-ratio of the 9.67RF mode rapidly diminishes to a negligible level. In contrast, the energy-ratio of the low-frequency mode (0.11RF) increases rapidly and becomes dominant.

### 4.2 Physical Explanations of Dominant Modes

To clarify the physical explanations of main single-frequency modes, the mode structures are analyzed by combining unsteady flow field distributions and Fast Fourier Transform (FFT) method.

Figure 12 shows the BPF mode structure of the compressor impeller at 95% span under the operating condition of 0.74kg/s. For convenience, the amplitude of mode is normalized to range from -1 to 1. The mode is primarily distributed at the outlet of the impeller flow passage and exhibits alternating maxima and minima in the circumferential direction, with one disturbance wave present in each passage. To clarify its physical explanation, the mode structure is analyzed by combining with transient flow field distributions.

Figure 13 presents the streamlines of the compressor at the moment $t$ ($t$=$t_0$+26$T$, $t_0$ is the moment of the first snapshot, $T$ is the rotor rotation period) under the 0.74kg/s operating condition. As shown in the figure, the fluid near the blade suction surface is influenced by the combined forces of centrifugal force and radial pressure difference, and exhibits a radial flow tendency. It moves from the blade hub to the blade tip, forming secondary flows along the blade surface. Under the interaction of the main flow, secondary flow, and blade tip leakage flow (BTLF), low-energy fluid accumulates in the wake region downstream, resulting in a jet-wake structure at the impeller outlet. The jet-wake structure is cut by diffuser vanes periodically, causing periodic variations at the inlet boundary of each diffuser passage. This is a typical phenomenon of rotor-stator interaction.

To further confirm that the BPF mode represents the rotor-stator interaction between the impeller and the diffuser, monitoring point is placed at the extrema of the BPF mode, as shown in Fig. 14(a). FFT analysis is performed on the unsteady static pressure data at this point, and the frequency spectrum is shown in Fig. 14(b). It is evident that BPF (8RF) completely dominates, with its amplitude significantly higher than other frequencies.

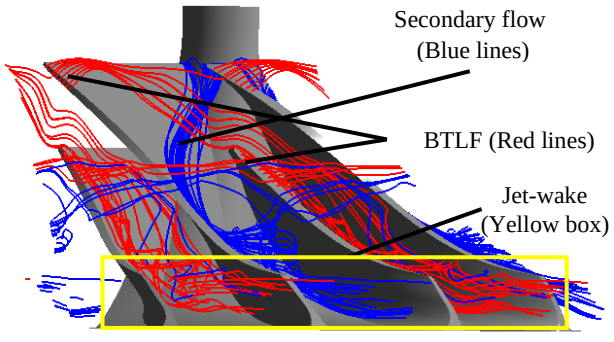


**Fig. 13 Streamlines of the compressor impeller at the moment *t* under the 0.74kg/s operating condition**

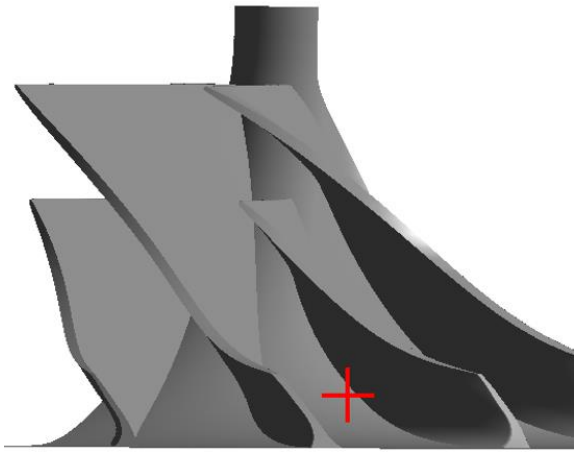

(a) location of the monitoring point

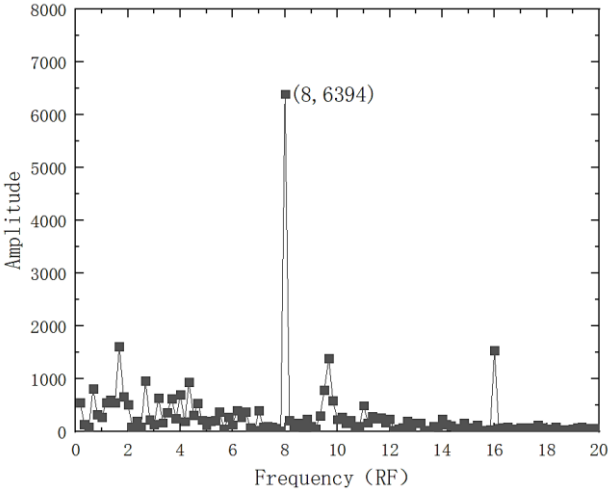


(b) FFT spectrum distribution

**Fig. 14 Location of monitoring point at the downstream and FFT spectrum distribution under the 0.74kg/s operating condition**

BPF and its harmonics have been detected in many studies, and most researchers attribute these frequencies to the rotor-stator interaction between impeller and vaned diffuser (Zamiri et al., 2017). Under the peak-efficiency condition, BPF is typically the dominant frequency of compressors. Therefore, BPF and its harmonics, representing rotor-stator interaction, can be considered as inherent mode of the compressor. Further analyses under different operating conditions of this compressor reveal that the mode structures of the BPF and its harmonics remains the same physical explanation, hence, they will not be discussed in further detail.

Next, the 9.67RF mode is investigated. Figure 15 presents the mode structure of the 9.67RF mode for the compressor impeller under the 0.74kg/s operating condition. This mode is primarily distributed near the leading edge of the blades and shows alternating maxima and minima in the circumferential direction. Its structure closely resembles that of the blade tip leakage vortex

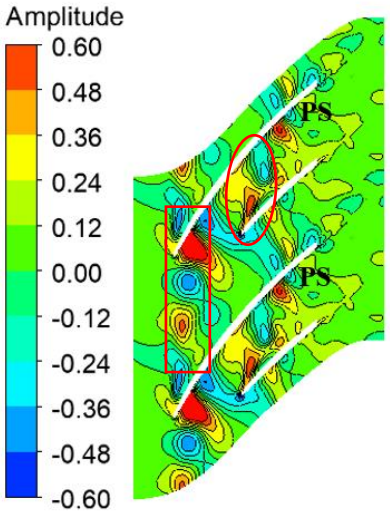


**Fig. 15 9.67RF mode structure of the compressor impeller under the 0.74kg/s operating condition**

(BTLV). Hence, it is preliminary assumed that this mode is related to BTLV.

To confirms this, Fig. 16 presents the vortex structures (obtained by Q-criterion) at different moments in the impeller under the 0.74kg/s operating condition. The time interval between adjacent moments is $\Delta t = 1/40T$ , where $T$ is the rotor rotation period. Combining the vortex structures in Fig. 16 and the streamlines in Fig. 13, it can be observed that the BTLF from the main blade tip clearance originates near the impeller inlet, and flows into the blade passage at a relatively small incidence angle. This leads to the formation of a BTLV and subsequent breakdown. The broken part moves downstream and reaches the pressure surface (PS) of the adjacent blade, corresponding to the 9.67RF mode structure shown in Fig. 15 (marked with red box). The vortexes from the splitter blade tip clearance show similar behaviors and correspond to the mode structure illustrated in Fig. 15 (marked with red ellipse).

To further analyze the relationship between the 9.67RF mode and the BTLV, a monitoring point is placed at the location shown in Fig. 17(a). FFT analysis is performed on the unsteady static pressure data at this point, and the frequency spectrum is shown in Fig. 17(b). It shows that the pressure pulsation at the blade tip clearance near the leading edge is dominated by the 9.67RF frequency, with other frequencies being negligible. Therefore, both the mode structure and the frequency spectrum confirm that the 9.67RF mode represents the breakdown of the BTLV.

As seen in Fig. 11, when the flow rate declines to 0.7kg/s, the energy-ratio of the 9.67RF mode decreases. The reasons for this are analyzed below. Figure 18 shows the 9.67RF mode structure of the compressor impeller at smaller flow rate operating condition (0.7kg/s). The structure is generally consistent with the 0.74kg/s operating condition (see Fig. 15). But there is a weakening of the amplitude of 9.67RF mode near the splitter blade

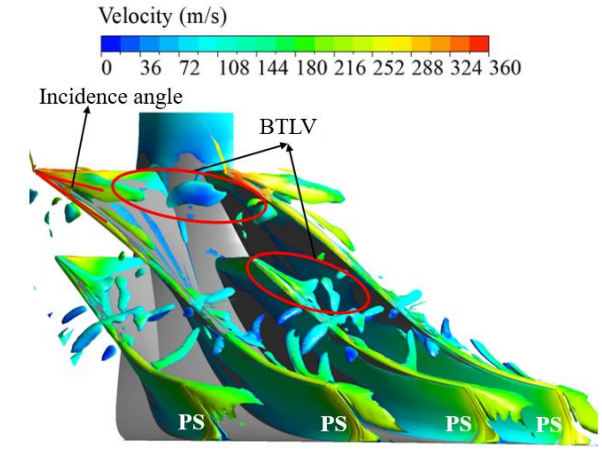


(a) $t$

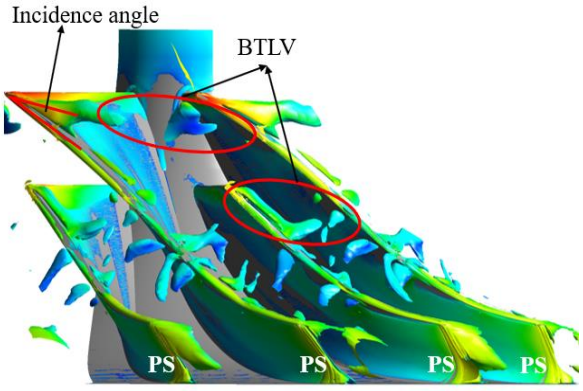


(b) $t+\Delta t$

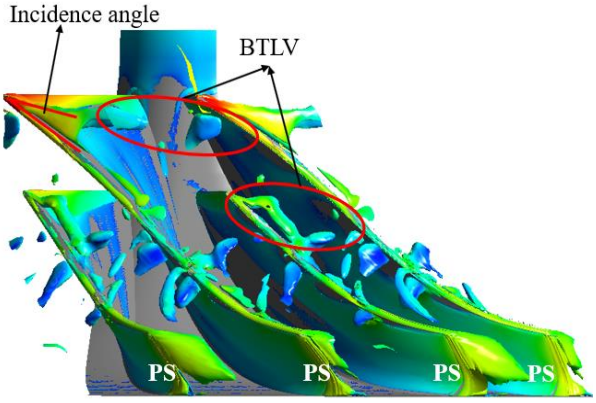


(c) $t+2\Delta t$

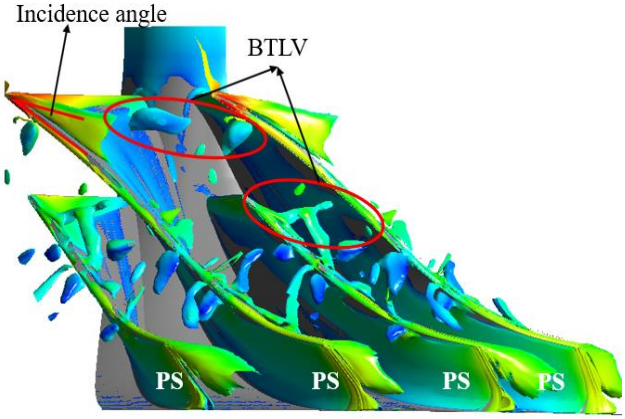


(d) $t+3\Delta t$

**Fig. 16 Impeller vortex structures at different moments under the 0.74kg/s operating condition**

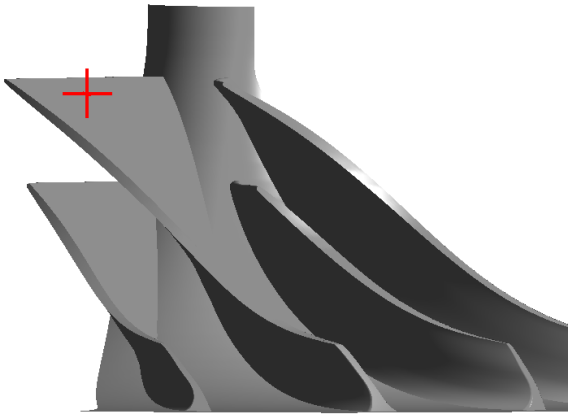

(a) location of the monitoring point

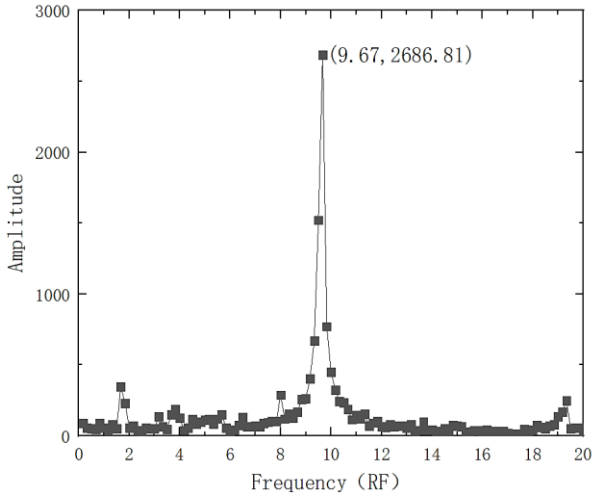


(b) FFT spectrum distribution

**Fig. 17 Location of monitoring point near the leading edge and FFT spectrum distribution under the 0.74kg/s operating condition**

leading edge and the downstream of blade passage, as shown in the red dotted ellipse. Additionally, the mode amplitude at the leading edge of the main blade increases as shown in the black dotted ellipse, which means an enhancement in pressure pulsation in this region.

Figure 19 shows the streamlines at moment $t$ for the compressor impeller under the 0.7kg/s operating condition. Figure 20 illustrates the impeller vortex structures at different moments under this operating condition. By combining Fig. 16 and 18, it is found that the BTLV breaks down due to a higher back pressure, and forms a passage vortex (PV). The passage vortex stretches perpendicular to the main flow direction, and almost occupies the entire blade passage, resulting in a blockage in blade passage. Then, the tip leakage flow is forced to bypass the leading edge of the adjacent main blade and flow into the next blade passage, resulting in a phenomenon known as leading-edge spillage. This suggests that the impeller has entered an unstable state. Compared to the 0.74kg/s operating condition (see Fig. 16), the incidence angle of BTLV has significantly

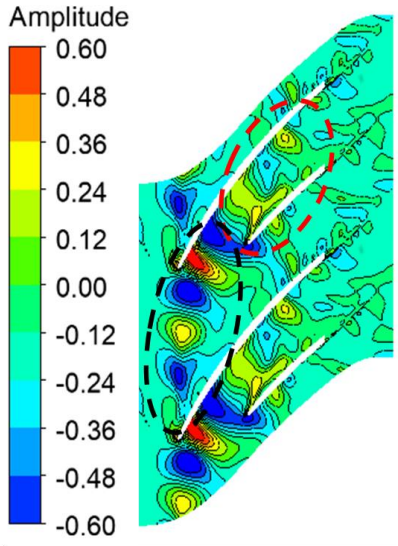


**Fig. 18 9.67RF mode of the compressor impeller under the 0.7kg/s operating condition**

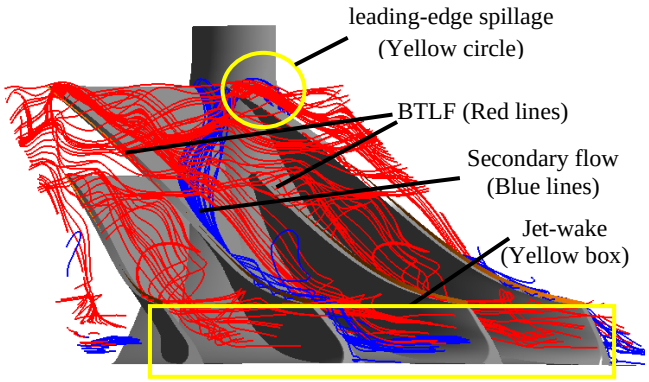


**Fig. 19 Streamlines of the compressor impeller at the moment *t* under the 0.7kg/s operating condition**

increased and the vortex direction has become almost parallel to the impeller inlet. But the BTLV intensity of splitter blade is significantly reduced. These flow patterns variations correspond to the mode amplitude variations in Fig. 15 and 18. Therefore, the 9.67RF mode under the 0.7kg/s operating condition still represents the BTLV. However, due to the breakdown of the BTLV, broadband multi-scale flow structures will be generated, leading to some changes in modes frequencies, and a decrease in 9.67RF mode energy-ratio.

To conclude, there are three primary reasons for the rapid reduction in the energy-ratio of the 9.67RF mode as the flow rate decreases. Firstly, there is a notable reduction in the intensity of the BTLV of the splitter blades, resulting in a lower mode amplitude in this region. Secondly, due to the higher back pressure, the breakdown of BTLV becomes much more significant, more broadband multi-scale flow structures have been generated, resulting in some variations in modes frequencies, and a decrease in 9.67RF mode energy-ratio. Finally, the energy-ratio

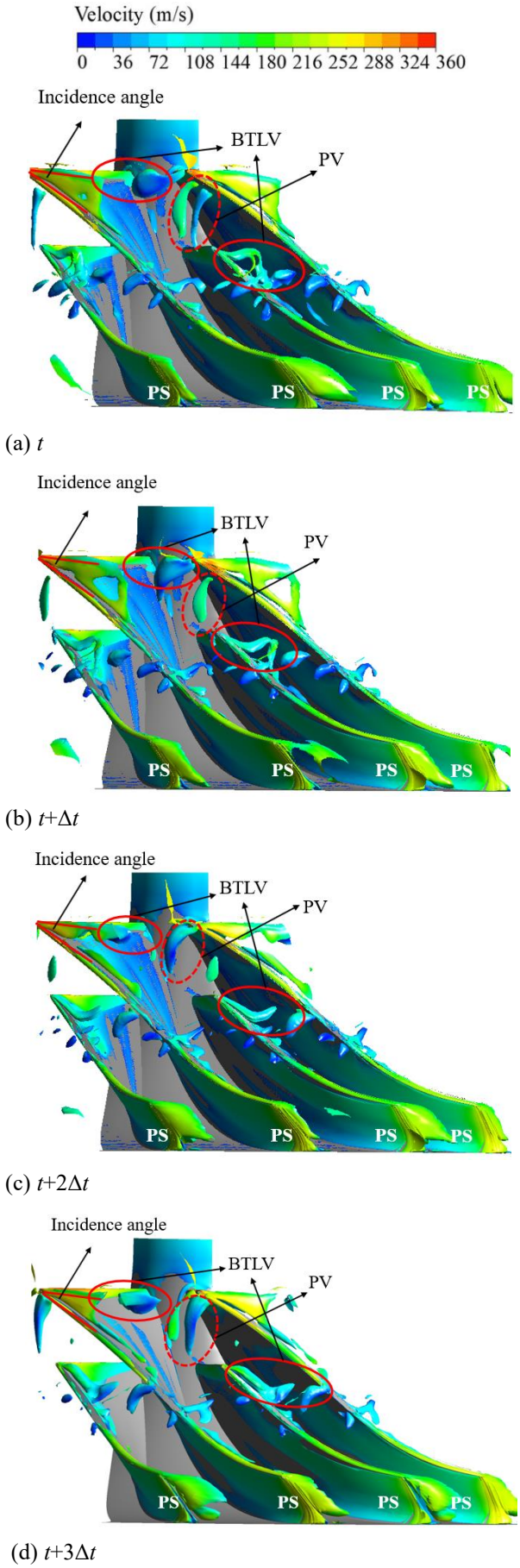


**Fig. 20 Impeller vortex structures at different moments under the 0.7kg/s operating condition**

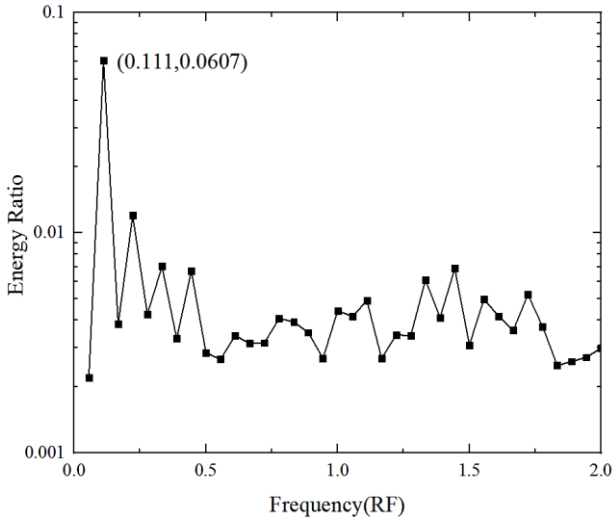


**Fig. 21 Mode decomposition results with doubled samples under the 0.7kg/s operating condition**

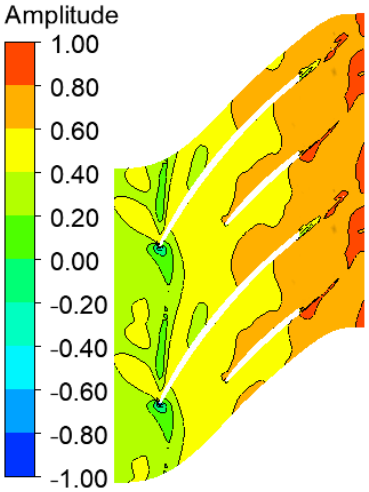


**Fig. 22 0.11RF mode of the compressor impeller under the 0.7kg/s operating condition**

of the 0.11RF mode increases rapidly, effectively reducing the energy-ratios of other modes.

Then, the physical explanation of the 0.11RF mode, and the reasons for its rapid increase in energy-ratio as the flow rate decreases are investigated. Since 0.11RF is the lowest resolvable frequency in the mode decomposition results, to examine whether the sampling resolution affects the DMD results, the quantity of samples in the mode decomposition increases twofold. This reduces the minimum resolution to 0.056RF. Figure 21 shows the mode decomposition results (0~2RF) for the 0.7kg/s operating condition with the increased number of samples. It can be seen that the mode with the largest energy-ratio is indeed 0.11RF, while the energy-ratio of the 0.055RF mode is almost negligible. This confirms that the sampling period meets the minimum resolution requirement and is sufficient to identify the primary flow structures.

Figure 22 shows the 0.11RF mode structure at the 0.7kg/s operating condition for the compressor impeller. It can be seen that the regions with the largest amplitude are mainly distributed downstream of the blade passage and at the impeller outlet. It is preliminarily hypothesized that this mode represents large-scale low-frequency disturbances downstream of the impeller, which dominate the global periodic fluctuations of the compressor flow field. Next, this region will be further studied to clarify its physical explanation.

Figure 23 shows the isentropic efficiency variations over the time of the compressor at the 0.7kg/s operating condition. The figure shows that the isentropic efficiency exhibits significant quasi-periodic fluctuations over the time. This indicates that the compressor is exhibiting strong unsteady characteristics, suggesting that the impeller has entered an unstable state. Figure 24 presents the total pressure variation over the time at the monitoring point located at the impeller outlet, as illustrated in Fig. 14(a). It is evident that the pressure fluctuation period matches that of the isentropic efficiency. Based on the time-varying curves of the variables, it is clear that one

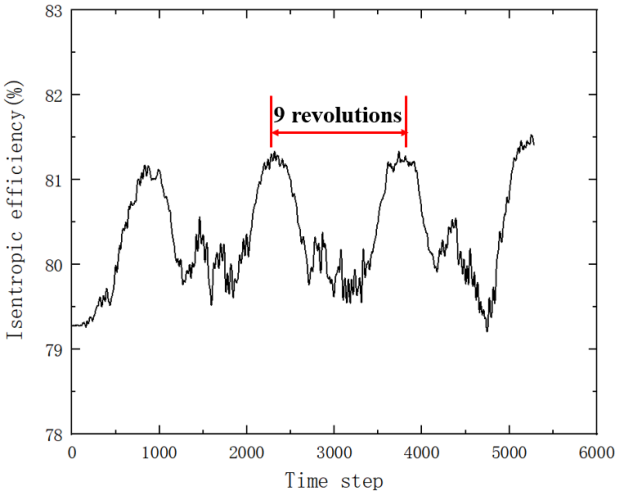


**Fig. 23 Isentropic efficiency variations over the time of the compressor under the 0.7kg/s operating condition**

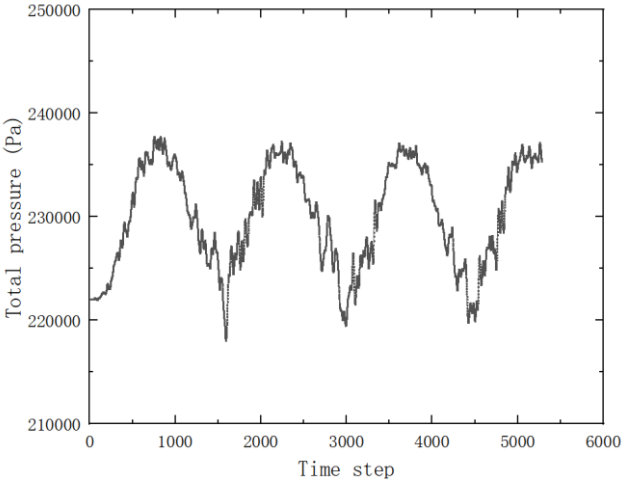


**Fig. 24 Total pressure variation at the monitoring point under the 0.7kg/s operating condition**

period of flow field fluctuation corresponds to 9 rotor rotations. Given a rotor speed of 50,000 rpm, the calculated frequency is: 50000/60/9=92.59 Hz. This precisely matches the frequency of the 0.11RF mode, confirming that the physical explanation of the 0.11RF mode represents large-scale low-frequency disturbances downstream of the impeller. It causes periodic fluctuations in the downstream flow field and dominates the periodic fluctuations of the compressor aerodynamic performances.

In summary, the BPF mode and its harmonics represent rotor-stator interactions in the compressor, with a significant energy-ratio across the entire operating range. Although its energy-ratio decreases with throttling process, it still plays a major role at low flow rates and can be defined as an inherent mode of the compressor. The 9.67RF mode represents the breakdown of the BTLV, with its energy-ratio rapidly decreasing as the flow rate decreases. As the flow rate reaches 0.65kg/s, its energy-ratio becomes negligible, meaning that it neither represents an inherent mode of the compressor nor a sign of compressor instability. The 0.11RF mode characterizes large-scale low-frequency disturbances downstream of the impeller as the flow rate decreases, leading to periodic fluctuations of overall aerodynamic performances. As the compressor throttles to the point of flow instability, the energy-ratio of this mode rapidly increases and becomes the dominant mode, thus defining it as a characteristic mode.

Based on the above studies, an optimization method for improving flow stability of centrifugal compressors based on the mode energy regulation of flow field is proposed. The optimization goal is to maximize the energy-ratio of the inherent mode and minimize the energy-ratio of the characteristic mode, while also considering performance indicators such as efficiency and pressure ratio. For the compressor in this study, the optimization design is conducted with the objective of maximizing the energy-ratio of the BPF mode and minimizing the energy-ratio of the 0.11RF mode.

## 5. COMPRESSOR OPTIMIZATION BASED ON MODE ENERGY REGULATION

### 5.1 Optimization Design Space

An optimization of the compressor based on dynamic mode energy regulation is carried out to improve the flow stability and maintain the aerodynamic performances. In the optimization, the stable operating range is intended to be improved, which means that both the stall margin and the choke margin of the compressor should be improved. To enhance the compressor stall margin, the energy ratio of inherent modes $E_{\mathrm{I}}$ is maximized, and the energy ratio of characteristic modes $E_C$ is minimized at the 0.7kg/s operating condition. To improve the choke margin, the choke mass flow rate $m_{\mathrm{choke}}$ is maximized. To maintain the aerodynamic performances of the compressor, the pressure ratios and efficiencies at the 0.74kg/s and the 0.7kg/s operating conditions ( $\varepsilon_{0.74\mathrm{kg/s}}$ , $\varepsilon_{0.7\mathrm{kg/s}}$ , $\eta_{0.74\mathrm{kg/s}}$ , $\eta_{0.7\mathrm{kg/s}}$ ) are constrained to be larger than the baseline values. The mathematical description of the optimization is expressed as follows:

$$\begin{aligned}
&\max:\ E_{\mathrm{I,\,0.7kg/s}},\, m_{\mathrm{choke}}\\
&\min:\ E_{\mathrm{C,\,0.7kg/s}}\\
&\text{s.t.}\begin{cases}
\varepsilon_{0.74\mathrm{kg/s}} \geq \varepsilon_{0.74\mathrm{kg/s,\,baseline}}\\
\varepsilon_{0.7\mathrm{kg/s}} \geq \varepsilon_{0.7\mathrm{kg/s,\,baseline}}\\
\eta_{0.74\mathrm{kg/s}} \geq \eta_{0.74\mathrm{kg/s,\,baseline}}\\
\eta_{0.7\mathrm{kg/s}} \geq \eta_{0.7\mathrm{kg/s,\,baseline}}
\end{cases}
\end{aligned} \tag{19}$$

To achieve the optimization objectives, the selection of design variables is important. Since the compressor stability (stall margin) is primarily determined by the impeller (see Fig. 7), the design variables associated with the impeller flow stability should be included. As suggested by the reference (Li et al., 2022), the impeller outlet tip blade angle and impeller main blade sweep angle are related to the impeller flow stability, hence, they are chosen as the design variables. On the other hand, to improve the choke margin, the design variables that dominate the flow capacity of the compressor should be considered. As indicated in the reference (Zhou et al., 2025), the diffuser vane angle and the vaned diffuser outlet radius mainly determine the solidity of the diffuser and have large effect on compressor choke margin. Therefore, these two design variables of the diffuser are selected. Actually, the existing study (Liu et al., 2024) has showed that the above four selected design variables can also impact the aerodynamic performances of compressor at various operating conditions. Hence, optimizing the four design variables has the potential to improve the stable operating range and maintain the aerodynamic performances of the compressor. To avoid a too complex design space of the optimization, no more design variables of the compressor are considered.

In terms of the varying ranges of the design variables, the single-parameter analysis is conducted to identify the beneficial variation ranges of each design variable for optimization objectives. The varying range of a design variable that leads to no improvement for all objectives is discarded. Also, the varying range resulting in severe geometric distortions for the compressor is also not considered.

**Table 3 Compressor optimization variables and design levels**

| Levels | Impeller main blade sweep angle A/deg | Impeller outlet tip blade angle B/deg | Vaned diffuser outlet radius C/mm | Diffuser vane angle D/deg |
|---|---|---|---|---|
| 1 | 1.75 | -36 | 97 | 60 |
| 2 | 3.75 | -40 | 103.5 | 61.5 |
| 3 | 5.75 | -44 | 110 | 63 |

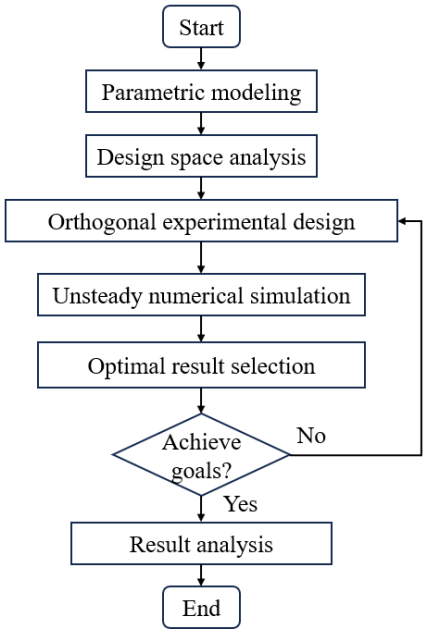


**Fig. 25 Process of optimization design**

### 5.2 Optimization Implementation

In the compressor optimization, the objectives related to flow stability ( $E_I$ , $E_C$ ) requires to evaluate the dynamic mode energy of the unsteady flow fields of the compressor, which needs substantial computational costs. Hence, it is necessary to consider the number of unsteady simulations of the compressor when selecting optimizers. Whether it is the stochastic algorithm or the gradient descent algorithm, a large number of samples are required for unsteady simulations. To save computational resources and time, this study adopts the orthogonal experimental design method and directly selects the optimal solution from the orthogonal array. It is likely to achieve a balance between the optimization effectiveness and optimization speed.

The optimization process is shown in Fig. 25. Firstly, the parametric modeling of the compressor is performed. Secondly, the design space is analyzed to determine the design objectives and constraints, as well as the design variables and their variation ranges. Then, an appropriate orthogonal array based on the number of design variables and their levels is designed. Next, unsteady numerical simulations are conducted for each design scheme in the orthogonal array. And then, all solutions are evaluated through comprehensive consideration of both optimization objectives and constraints, and to select the optimal solution. If the solution meets design requirements, the optimization is stop; if not, the orthogonal experiment is redesigned, and the loop is continued. Finally, the optimization results are analyzed.

**Table 4 Orthogonal experiment design table**

| Number | Scheme | Number | Scheme |
|---|---|---|---|
| 1 | $A_1B_1C_1D_1$ | 6 | $A_2B_3C_1D_2$ |
| 2 | $A_1B_2C_2D_2$ | 7 | $A_3B_1C_3D_2$ |
| 3 | $A_1B_3C_3D_3$ | 8 | $A_3B_2C_1D_3$ |
| 4 | $A_2B_1C_2D_3$ | 9 | $A_3B_3C_2D_1$ |
| 5 | $A_2B_2C_3D_1$ | | |

An orthogonal experimental design method is used for the compressor optimization. Based on the initial values of design variables and considering their varying ranges, three levels of each design variable are determined, as shown in Table 3. In orthogonal experimental design, for an orthogonal array with 4 factors (design variables) and 3 levels, the most commonly used option is the $L_9(3^4)$ array (9 test runs). If higher-precision analysis is required, the levels of design variables can be increased, and then a larger orthogonal array may be selected (e.g., $L_{27}(3^n)$, where $n$ is the number of levels). To save computational resources and time, this study adopts the $L_9(3^4)$ orthogonal array. The orthogonal experiment design table is presented in Table 4, with a total of nine schemes.

For each design scheme in Table 4, numerical simulations are performed to obtain unsteady flow fields. DMD is applied to the unsteady flow fields to extract discrete frequency modes and their energy-ratios. The orthogonal experimental design results are presented in Table 5. The optimal scheme is selected by considering the inherent mode energy-ratio ($E_I$), characteristic mode energy-ratio ($E_C$) at the 0.7kg/s operating condition, and efficiency ($\eta$) and pressure ratio ($\varepsilon$) under both 0.74kg/s and 0.7kg/s operating conditions. As seen in Table 5, Scheme 4 has the highest inherent mode energy-ratio and

**Table 5 Results of the orthogonal experiment design**

| Number | $E_{I,\ 0.7kg/s}$ | $E_{C,\ 0.7kg/s}$ | $\eta_{0.74kg/s}$ (%) | $\varepsilon_{0.74kg/s}$ | $\eta_{0.7kg/s}$ (%) | $\varepsilon_{0.7kg/s}$ | $m_{choke}$ (kg/s) |
|---|---|---|---|---|---|---|---|
| 1 | 0.0502 | 0.06543 | 80.481 | 2.2371 | 78.749 | 2.2282 | 1.0858 |
| 2 | 0.0586 | 0.06887 | 81.489 | 2.2706 | 79.282 | 2.2183 | 1.0097 |
| 3 | 0.0607 | 0.06718 | 81.560 | 2.2569 | 79.893 | 2.2368 | 0.9640 |
| 4 | 0.0775 | 0.03812 | 82.084 | 2.3111 | 80.902 | 2.3031 | 1.0542 |
| 5 | 0.0507 | 0.04986 | 81.192 | 2.2663 | 79.100 | 2.2564 | 1.0336 |
| 6 | 0.0554 | 0.06762 | 81.168 | 2.2534 | 79.503 | 2.2573 | 1.0554 |
| 7 | 0.0553 | 0.07469 | 81.928 | 2.2727 | 80.097 | 2.2471 | 1.0133 |
| 8 | 0.0580 | 0.06061 | 81.348 | 2.2854 | 79.905 | 2.2768 | 1.0393 |
| 9 | 0.0508 | 0.04527 | 81.097 | 2.2848 | 79.273 | 2.2443 | 1.0374 |

**Table 6 Comparison of inherent and characteristic modes energy-ratios before and after optimization**

| | $E_I$ | $E_C$ |
|---|---|---|
| Baseline | 0.0618 | 0.0792 |
| Optimization | 0.0775 | 0.03812 |
| Improvements | +25.4% | -51.84% |

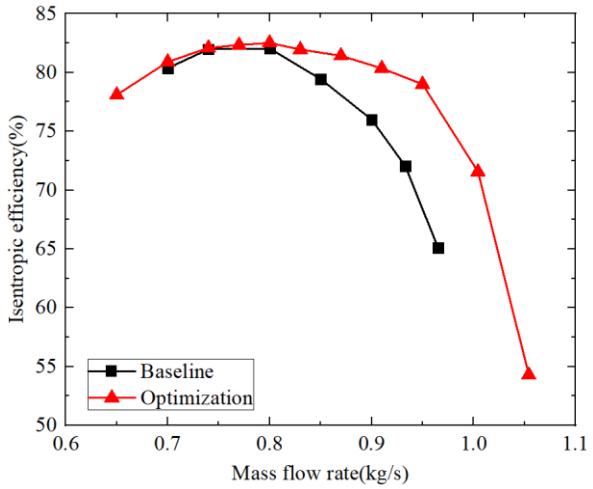


(a) isentropic efficiency

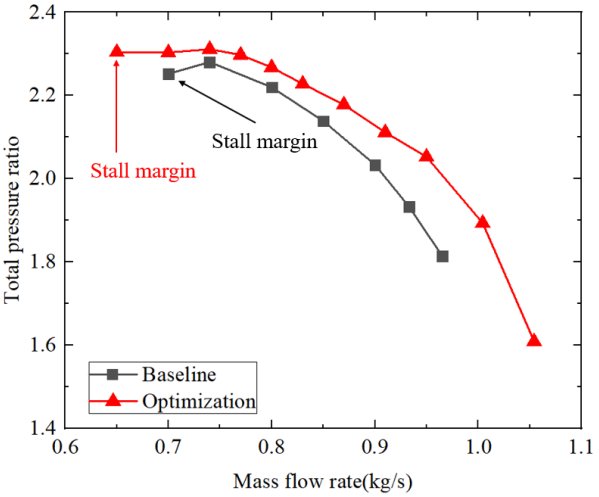


(b) total pressure ratio

**Fig. 26 Characteristic curves of the compressor before and after optimization**

the lowest characteristic mode energy-ratio. Also, it possesses a larger choke mass flow rate. Moreover, its efficiency and pressure ratio under both 0.74kg/s and 0.7kg/s operating conditions are higher than those of other schemes. So, Scheme 4 is chosen as the optimal solution.

Table 6 presents a comparison of the inherent and characteristic modes energy-ratios at the 0.7kg/s operating condition before and after optimization. It can be observed that after optimization, the energy-ratio of the characteristic mode (0.11RF), which is related to compressor instability, is significantly suppressed. And the energy-ratio of the inherent mode (BPF) is increased. Specifically, the inherent mode energy-ratio at the 0.7kg/s operating condition is increased by 25.4%, and the characteristic mode energy-ratio is decreased by 51.84%.

The characteristic curves of the compressor before and after optimization are shown in Fig. 26. It can be seen that the optimized compressor (Scheme 4) demonstrates improved aerodynamic performances across the entire operating range. At the same time, the stall flow rate is reduced by 8.45% and the choke flow rate is increased by 5.11%. This verifies the effectiveness of the optimization strategy based on energy transfer regulation of dynamic modes.

### 5.3 Mode Structures Analyses

After optimization, the stable operating range of the compressor is expanded while the aerodynamic performances are maintained across the entire operating range. To further demonstrate the feasibility of this method in principle, a comparative analysis of the mode structures before and after optimization is conducted.

Figure 27 presents a comparison of the 0.11RF mode structure at the 0.7kg/s operating condition before and after optimization. It can be observed that the large-scale low-frequency disturbances downstream of the impeller are significantly suppressed after optimization. As discussed in Eq. (16) of Section 3, the magnitude of the mode represents the mode energy. The unnormalized mode energy of 0.11RF is $3.62\times10^6$ before optimization, while it is $2.61\times10^6$ after optimization. This indicates that the mode energy is significantly suppressed.

Figure 28 compares the BPF mode structure at the 0.7kg/s operating condition before and after optimization. The figure shows that there is no significant change in the BPF mode after optimization, with the main extremum regions still concentrated at the impeller outlet. It is difficult to judge the energy change solely from the mode structure contour. However, by calculating the mode magnitude through Eq. (16), it is found that the unnormalized mode energy of BPF is $2.83\times10^6$ before optimization, and it is increased to $5.30\times10^6$ after

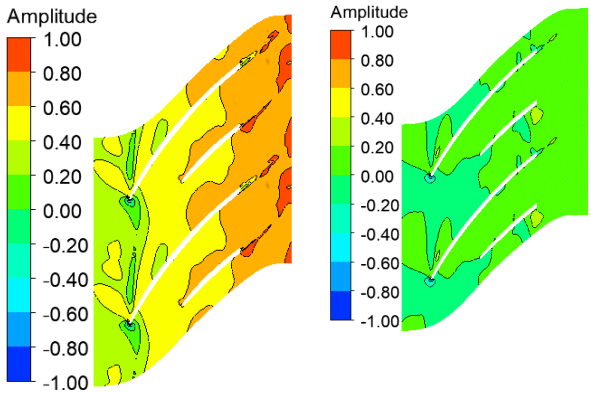


(a) baseline (b) optimization

**Fig. 27 Comparison of 0.11RF mode structures of the compressor impeller at 95% span under the 0.7kg/s operating condition before and after optimization**

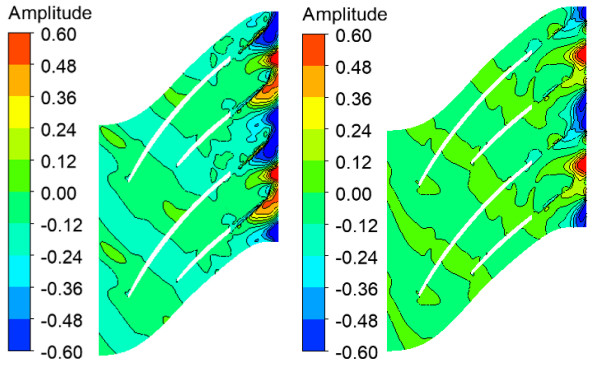


(a) baseline (b) optimization

**Fig. 28 Comparison of BPF mode structures of the compressor impeller at 95% span under the 0.7kg/s operating condition before and after optimization**

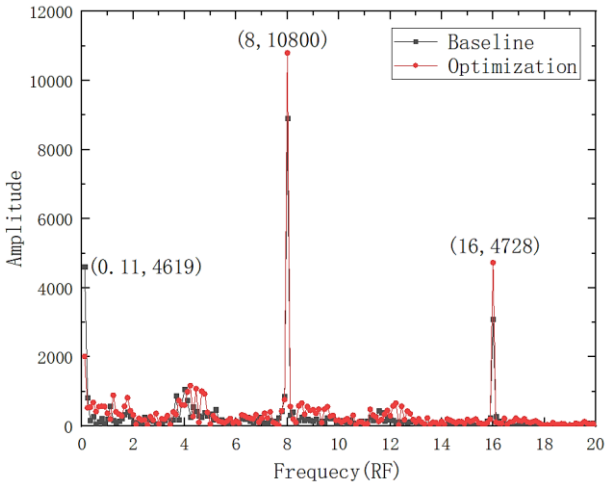


**Fig. 29 Comparison of FFT spectrum distributions of the static pressure at the monitoring point before and after optimization**

optimization. This shows that the BPF mode energy is significantly enhanced after optimization.

To further confirm the variations in mode energy, FFT analysis is performed on the static pressure over the time at the monitoring point marked in Fig. 14(a). The FFT results are presented in Fig. 29. It shows that the amplitude of the 0.11RF mode is decreased after optimization, while the amplitudes of the BPF and its harmonics are significantly increased. This further confirms that the inherent mode energy of the compressor is enhanced and the characteristic mode energy is suppressed after optimization, thereby improving the compressor flow stability.

## 6. CONCLUSIONS AND REMARKS

The global and unsteady mechanisms of flow instability of a centrifugal compressor are analyzed based on DMD method. Then an optimization method for improving flow stability based on dynamic mode energy regulation is proposed. The main conclusions are drawn as follows:

The baseline compressor exhibits three dominant modes: 0.11RF, BPF, and 9.67RF. Through analyzing the single-frequency modes structures and the corresponding unsteady flow fields distributions as well as FFT results, the physical explanations of dominant modes are elucidated. It is found that the 9.67RF mode represents the breakdown of the BTLV. Its energy-ratio decreases to negligible levels as the flow rate decreases, indicating that it neither represents an inherent characteristic of the compressor nor a sign of flow instability. The BPF mode represents rotor-stator interaction between the impeller and diffuser, and its energy-ratio remains dominant across the entire operating range. So, it is defined as an inherent mode of the compressor. The 0.11RF mode represents large-scale low-frequency disturbances downstream of the impeller. Its energy-ratio rapidly increases as the flow rate decreases, so it is defined as a characteristic mode, which is related to compressor flow instability.

When the compressor throttles to approach stall, the energy-ratio of the inherent mode gradually decreases, and that of the characteristic mode rapidly increases and becomes the dominant mode of the flow field. This indicates that the essence of compressor instability is the energy transfer from the inherent mode to the characteristic mode. Based on this mechanism, an optimization method is proposed to improve the flow stability of compressors while maintaining the aerodynamic performances through regulating energy transfer among dynamic modes.

The optimization results show that the energy-ratio of the inherent mode is increased by 25.4% and the energy-ratio of the characteristic mode is reduced by 51.84% at the 0.7kg/s operating condition. The compressor aerodynamic performances across the entire operating range are improved. The stall flow rate is reduced by 8.45% and the choke flow rate is increased by 5.11%. The principles of the optimization method are validated by analyzing the flow dynamic modes structures before and after optimization.

When the optimization methodology presented in this paper is applied to other compressors, the specific dominant frequencies will differ depending on individual compressor geometry and operating conditions. However, the rationale and procedure of the method are consistent. The procedure of this method could be further improved by incorporating small-sample machine learning as a surrogate model to enable efficient global optimization. Besides, the current optimization results lack experimental validation, which will be addressed in authors future work through aerodynamic performances and flow fields measurements of the optimized compressor.

## ACKNOWLEDGEMENTS

This study is funded by National Natural Science Foundation of China (Grant Nos. 12472238, 12372289 and 12472294), Tianjin Science and Technology Planning Project (Grant No. 24ZXZSSS00130) and Tianjin

Municipal Education Commission Research Project (Grant No. 2023KJ205).

## CONFLICT OF INTEREST

The authors declare that they have no known competing financial interests or personal relationships that could have appeared to influence the work reported in this paper.

## AUTHORS CONTRIBUTION

**X. A. Xie:** Conceptualization, Data curation, Investigation, Methodology, Software, Visualization, Formal analysis, Writing original draft. **Z. X. Liu:** Methodology, Formal analysis, Resources. **X. J. Li:** Conceptualization, Methodology, Supervision, Writing review & editing. **M. Zhao:** Validation, Formal Analysis. **Y. J. Zhao:** Software, Writing review & editing.

## REFERENCES

Ansys. (2011). *ANSYS CFX-solver theory guide*. ANSYS Inc.

Bagheri, S. (2013). Koopman-mode decomposition of the cylinder wake. *Journal of Fluid Mechanics*, *726*, 596-623. https://doi.org/10.1017/jfm.2013.249

Bitikofer, C., Schoen, M. P., Li, J. C., & Lin, F. (2017). *Characteristic Moore-Greitzer model parameter identification for a one stage axial compressor system*. 2017 American Control Conference (ACC), (pp. 164-169). IEEE. https://doi.org/10.23919/ACC.2017.7962948

Broatch, A., García-Tíscar, J. O. R. G. E., Roig, F., & Sharma, S. (2019). Dynamic mode decomposition of the acoustic field in radial compressors. *Aerospace Science and Technology*, *90*, 388-400. https://doi.org/10.1016/j.ast.2019.05.015

Cameron, J. D., Bennington, M. A., Ross, M. H., Morris, S. C., Du, J., Lin, F., & Chen, J. (2013). The influence of tip clearance momentum flux on stall inception in a high-speed axial compressor. *Journal of Turbomachinery*, *135*(5), 051005. https://doi.org/10.1115/1.4007800

Cheng, F., Sun, D., Dong, X., & Sun, X. (2017). Prediction of stall inception in multi-stage compressors based on an eigenvalue approach. *Science China Technological Sciences*, *60*(8), 1132-1143. https://doi.org/10.1007/s11431-016-0355-3

Cumpsty, N. A. (2004). *Compressor aerodynamics*. Krieger Publishing.

Day, I. J. (2016). Stall, surge, and 75 years of research. *Journal of Turbomachinery*, *138*(1), 011001. https://doi.org/10.1115/1.4031473

Dong, X., Sun, D., Li, F., & Sun, X. (2018). Stall margin enhancement of a novel casing treatment subjected to circumferential pressure distortion. *Aerospace Science and Technology*, *73*, 239-255. https://doi.org/10.1016/j.ast.2017.12.005

Fu, L., Hu, C., Yang, C., Bao, W., & Zhou, M (2020). Vortex trajectory prediction and mode analysis of compressor stall with strong non-uniformity. *Aerospace Science and Technology*, *105*, 106031. https://doi.org/10.1016/j.ast.2020.106031

Fujisawa, N., Inui, T., & Ohta, Y. (2019). Evolution process of diffuser stall in a centrifugal compressor with vaned diffuser. *Journal of Turbomachinery*, *141*(4), 041009. https://doi.org/10.1115/1.4042249

Grondin, J., Trébinjac, I., & Rochuon, N. (2018). Rotating instabilities versus rotating stall in a high-speed centrifugal compressor. *Turbo Expo: Power for Land, Sea, and Air*, V02BT44A025. https://doi.org/10.1115/GT2018-76916

Hong, S., Huang, G., Yang, Y., & Liu, Z. (2018). Introduction of DMD method to study the dynamic structures of a three-dimensional centrifugal compressor with and without flow control. *Energies*, *11*(11), 3098. https://doi.org/10.3390/en11113098

Hosseinimaab, S. M., & Tousi, A. M. (2022). Optimizing the performance of a single-shaft micro gas turbine engine by modifying its centrifugal compressor design. *Energy Conversion and Management*, *271*, 116245. https://doi.org/10.1016/j.enconman.2022.116245

Hu, C., Yang, C., Yi, W., Hadzic, K., Xie, L., Zou, R., & Zhou, M. (2020a). Numerical investigation of centrifugal compressor stall with compressed dynamic mode decomposition. *Aerospace Science and Technology*, *106*, 106153. https://doi.org/10.1016/j.ast.2020.106153

Hu, C., Yang, C., Yi, W., Zheng, S., Zou, R., & Zhou, M. (2020b). Influence of shroud profiling on the compressor diffuser: Frozen-eddy approach and mode decomposition. *International Journal of Mechanical Sciences*, *178*, 105623. https://doi.org/10.1016/j.ijmecsci.2020.105623

Huang, S., Yang, C., Han, G., Zhao, S., & Lu, X. (2020). Multipoint design optimization for a controlled diffusion airfoil compressor cascade. *Proceedings of the Institution of Mechanical Engineers, Part C: Journal of Mechanical Engineering Science*, *234*(11), 2143-2159. https://doi.org/10.1177/0954406220904

Kou, J., & Zhang, W. (2017). An improved criterion to select dominant modes from dynamic mode decomposition. *European Journal of Mechanics-B/Fluids*, *62*, 109-129. https://doi.org/10.1016/j.euromechflu.2016.11.015

Li, C. Y., Chen, Z., Zhang, X., Tim, K. T., & Lin, C. (2023). Koopman analysis by the dynamic mode decomposition in wind engineering. *Journal of Wind Engineering and Industrial Aerodynamics*, *232*,

105295. https://doi.org/10.1016/j.jweia.2022.105295

Li, C., Bin, G., Li, J., & Liu, Z. (2021). Study on the erosive wear of the gas-solid flow of compressor blade in an aero-turboshaft engine based on the Finnie model. *Tribology International*, *163*, 107197. https://doi.org/10.1016/j.triboint.2021.107197

Li, X., Liu, Z., Zhao, M., Zhao, Y., & He, Y. (2022). Stability improvement without efficiency penalty of a transonic centrifugal compressor by casing treatment and impeller/diffuser coupling optimization. *Aerospace Science and Technology*, *127*, 107685. https://doi.org/10.1016/j.ast.2022.107685

Liu, X., Sun, D., & Sun, X. (2014). Basic studies of flow-instability inception in axial compressors using eigenvalue method. *Journal of Fluids Engineering*, *136*(3), 644-649. https://doi.org/10.1115/1.4026417

Liu, X., Zhou, Y., Sun, X., & Sun, D. (2015). Calculation of flow instability inception in high speed axial compressors based on an eigenvalue theory. *Journal of Turbomachinery*, *137*(6), 061007. https://doi.org/10.1115/1.4028768

Liu, Z., Xie, X., & Li, X. (2024). A coupling optimisation strategy for improving flow stability and aerodynamic performances of turbocharger centrifugal compressors. *International Journal of Automotive Technology*, 1-15. https://doi.org/10.1007/s12239-024-00185-6.

Schmid, P. J. (2010). Dynamic mode decomposition of numerical and experimental data. *Journal of Fluid Mechanics*, *656*, 5-28. https://doi.org/10.1017/S0022112010001217

Shu, M., Yang, M., Deng, K., Zheng, X., & Martinez-Botas, R. F. (2018). Performance analysis of a centrifugal compressor based on circumferential flow distortion induced by volute. *Journal of Engineering for Gas Turbines and Power*, *140*(12), 122603. https://doi.org/10.1115/1.4040681

Stein, T., Leitner, M. W., & Staudacher, S. (2025). Effect of leading edge erosion on the tip leakage flow in a compressor cascade. *Journal of Turbomachinery*, *147*(8), 081015. https://doi.org/10.1115/1.4067462

Sun, X., Liu, X., Hou, R., & Sun, D. (2013). A general theory of flow-instability inception in turbomachinery. *AIAA Journal*, *51*(7), 1675-1687. https://doi.org/10.2514/1.J052186

Taira, K., Brunton, S. L., Dawson, S. T., Rowley, C. W., Colonius, T., McKeon, B. J., Schmidt, O. T., Gordeyev, S., Theofilis, V., & Ukeiley, L. S. (2017). Mode analysis of fluid flows: An overview. *AIAA Journal*, *55*(12), 4013-4041. https://doi.org/10.2514/1.J056060

Vo, H. D., Tan, C. S., & Greitzer, E. M. (2005, January). *Criteria for spike initiated rotating stall*. Turbo Expo: Power for Land, Sea, and Air (Vol. 47306, pp. 155-165). https://doi.org/10.1115/GT2005-68374

Wilson, K. (2024). *Modeling and control design for one stage axial flow compressor*. Idaho State University.

Wu, Z., Brunton, S. L., & Revzen, S. (2021). Challenges in dynamic mode decomposition. *Journal of the Royal Society Interface*, *18*(185), 20210686. https://doi.org/10.1098/rsif.2021.0686

Xu, L., Liu, Z., Li, X., Zhao, M., Zhao, Y., & Zhou, T. (2023). Dynamic mode characteristics of flow instabilities in a centrifugal compressor impeller. *Aerospace Science and Technology*, *142*, 108707. https://doi.org/10.1016/j.ast.2023.108707

Xu, R., Sun, D., Dong, X., Li, F., Sun, X., & Li, J. (2019). Application of stall warning approach with stall precursor-suppressed casing treatment on a two-stage compressor. *Journal of Thermal Science*, *28*, 862-874. https://doi.org/10.1007/s11630-019-1186-5

Xu, D., Dong, X., Xu, R., Li, J., Sun, D., & Sun, X. (2022). Research progress of adaptive control methods for compressor flow stability. *Chinese Journal of Theoretical and Applied Mechanics*, *54* (3), 559-576. https://doi.org/10.6052/0459-1879-21-560

Xue, X., & Tong, W. (2019). Experimental and computational analysis of the unstable flow structure in a centrifugal compressor with a vaneless diffuser. *Chinese Journal of Mechanical Engineering*, *32*(1), 1-13. https://doi.org/10.1186/s10033-019-0379-x

Xue, X., Wang, T., Shao, Y., Yang, B., & Gu, C. (2019). Experimental and numerical analysis of different unsteady modes in a centrifugal compressor with variable vaned diffuser. *Journal of Fluids Engineering*, *141*(10), 101106. https://doi.org/10.1115/1.4043273

Yang, M., Shu, M., Yang, B., Martinez-Botas, R., & Deng, K. (2022). Unsteady response of performance for centrifugal compressor under pulsating backpressure condition. *Aerospace Science and Technology*, *126*, 107589. https://doi.org/10.1016/j.ast.2022.107589

Zamiri, A., Lee, B. J., & Chung, J. T. (2017). Numerical evaluation of transient flow characteristics in a transonic centrifugal compressor with vaned diffuser. *Aerospace Science and Technology*, *70*, 244-256. https://doi.org/10.1016/j.ast.2017.08.003

Zhang, M., Wu, W., & Zhou, C. (2023). Numerical model of predicting surge boundaries in high-speed centrifugal compressors. *Aerospace Science and Technology*, *141*, 108518. https://doi.org/10.1016/j.ast.2023.108518

Zhang, Y., Lu, X., Zhang, Y., Zhang, Z., Dong, X., & Han, G. (2022). Stall behavior in an ultrahigh-pressure-ratio centrifugal compressor: Backward-traveling rotating stall. *Journal of Turbomachinery*, *144*(10), 101010. https://doi.org/10.1115/1.4050918

Zhao, Y., Liu, Z., Fu, L., Zhao, M., & Li, X. (2023). Redesign of a turbocharger compressor based on multi-component full-passage optimization. *Aerospace Science and Technology*, *142*, 108644. https://doi.org/10.1016/j.ast.2023.108644

Zhou, T., Liu, Z., Li, X., Zhao, M., Zhao, Y., & Xu, L. (2025). Unsteady flow mechanisms of the stability improvement for an optimized compressor. *Journal of Applied Fluid Mechanics*, *18*(4), 919-932. 10.47176/jafm.18.4.3056

Zhu, X., Hu, C., Yang, X., & Du, Z. (2019). Dynamic mode decomposition analysis of the unsteady flow in a centrifugal compressor volute. *Journal of Aerospace Engineering*, *32*(1), 04018136. https://doi.org/10.1061/(ASCE)AS.1943-5525.00009